

Electromechanical Finite Elements

For magnetic actuators and sensors, mechanical parameters usually influence performance more than any other nonelectromagnetic parameters. For example, armature mass directly affects the speed of response of a magnetic actuator. Mechanical and electromagnetic behaviors are coupled together and described as *electromechanical* behavior.

This chapter and the next are devoted to electromechanical analysis. The present chapter uses electromechanical finite elements to analyze the behavior of magnetic actuators and sensors.

14.1 ELECTROMAGNETIC FINITE-ELEMENT MATRIX EQUATION

The magnetic finite elements described in Chapter 4 are not sufficient by themselves to completely analyze magnetic actuators and sensors. Subsequent chapters have described the use of finite elements to analyze electric fields and coupled electromagnetic fields. In addition, the electric circuit exciting the actuator or sensor must be included in many analyses.

An electromagnetic finite-element formulation that is capable of analyzing all types of electromagnetic fields is described here. While many other formulations exist, each with its own advantages, the formulation given here is easy to understand and is directly related to the structural finite-element formulation to follow.

As Chapter 4 showed, an energy functional can be used to derive a finite-element matrix equation. In Chapter 4 the functional consisted of magnetic energy and input electrical energy for magnetostatic finite elements. Here for electromagnetic finite elements that include not only magnetostatic energy, but also eddy current power loss, electrostatic energy, and coupled electromagnetic field energy, additional terms must be added. Here instead of minimizing an energy functional w by setting its derivative with respect to an unknown potential p to zero, we set the differential

energy variational δw to zero. The complete electromagnetic energy variational is [1]:

$$\begin{aligned}
 \delta w = & \int_{\text{vol}} dv \int_{t_o} dt \left\{ \left[\delta \left(\nabla \frac{\partial \psi}{\partial t} \right) + \delta \frac{\partial \mathbf{A}}{\partial t} \right] \cdot [\varepsilon] \left(\nabla \frac{\partial \psi}{\partial t} + \frac{\partial \mathbf{A}}{\partial t} \right) \right. \\
 & - [\delta (\nabla \psi) + \delta \mathbf{A}] \cdot [\sigma] \left(\nabla \frac{\partial \psi}{\partial t} + \frac{\partial \mathbf{A}}{\partial t} \right) - \delta (\nabla \times \mathbf{A}) \cdot [\nu] (\nabla \times \mathbf{A}) \\
 & \left. - \alpha \delta [\nu] (\nabla \cdot \mathbf{A}) \cdot (\nabla \cdot \mathbf{A}) - \delta \psi (\rho_v) + \delta \mathbf{A} \cdot \mathbf{J} \right\} \\
 & + \int_{\text{surf}} ds \int_{t_o} dt \left[\delta \mathbf{A} \cdot (\mathbf{H} \times \mathbf{u}_n) - \delta \psi \left(\mathbf{u}_n \cdot \left(\mathbf{J} + \frac{\partial \mathbf{D}}{\partial t} \right) \right) \right] \\
 & + \int_{\text{surf}} ds \delta \Psi (\mathbf{u}_n \cdot \mathbf{D})|_{t_o}
 \end{aligned} \tag{14.1}$$

where the potential component Ψ is the time integral of the electric scalar potential ϕ_v of (2.39), that is:

$$\Psi = \int dt \phi_v \tag{14.2}$$

The first right-hand side energy term in (14.1) is due to stored electric energy, the second term is energy lost due to eddy currents and other conduction currents, and the third is due to stored magnetic energy. The fourth term imposes uniqueness on 3D magnetic vector potential \mathbf{A} by penalizing its divergence by a factor α , and is needed only for 3D nodal finite elements; the 3D tangential vector (edge) elements mentioned in Chapter 4 do not require this term (nor do 2D or axisymmetric elements). The fifth and sixth terms represent volume energy excitations on potential components Ψ and \mathbf{A} , respectively. The final surface integral terms (with unit vector normal to the surface) allow energy to be input through the boundaries of the finite-element model.

The 3D electromagnetic finite-element formulation derived by setting the energy variational of (14.1) to zero contains three matrices: $[K_E]$, $[B_E]$, and $[M_E]$. They appear in the electromagnetic finite-element equation [1, 2]:

$$[M_E]\{\ddot{u}_E\} + [B_E]\{\dot{u}_E\} + [K_E]\{u_E\} = \{F_E(t)\} \tag{14.3}$$

where $[K_E]$ is the reluctance stiffness matrix of (4.13) and is here defined in terms of shape functions N by the finite-element volume integral:

$$[K_E] = \int dv [\nabla \times N]^T [v] [\nabla \times N] \quad (14.4)$$

where the central factor, the reluctivity tensor matrix, is the inverse of the magnetic permeability tensor matrix $[\mu]$. The $[B_E]$ matrix of (14.3) is called the conductance matrix and is proportional to the conductivity tensor according to:

$$[B_E] = \int dv [\nabla N]^T [\sigma] [\nabla N] \quad (14.5)$$

and accounts for energy (power) loss necessary to solve eddy current problems. Finally, to solve problems where electric field energy storage is included, the permittance matrix proportional to permittivity is defined as:

$$[M_E] = \int dv [\nabla N]^T [\epsilon] [\nabla N] \quad (14.6)$$

and is needed in coupled electromagnetic problems.

The unknown electromagnetic vector $\{u_E\}$ in (14.3) contains in general four components at each finite-element node:

$$\{u_E\} = \begin{bmatrix} A_1 \\ A_2 \\ A_3 \\ \Psi \end{bmatrix} \quad (14.7)$$

where the three components of magnetic vector potential \mathbf{A} in many cases are x , y , and z components, but may also be in other coordinate systems (global or elemental).

The right-hand side of (14.3) is the electromagnetic excitation vector:

$$\{F_E\} = \left[\begin{array}{c} J_{\text{vector}} \\ 0 \end{array} \right] \Big|_{\text{node}} + \left[\begin{array}{c} H_{\text{tan}} \\ J_{\text{norm}} \end{array} \right] \Big|_{\text{surface}} + \left[\begin{array}{c} \nabla \times \mathbf{H}_c \\ 0 \end{array} \right] \Big|_{\text{volume}} \quad (14.8)$$

where the vector J_{vector} includes the current densities at the finite-element nodes as described in two dimensions in (4.12), but here allowing for all 3D components. The second term in (14.8) allows for 3D \mathbf{H} fields to be imposed on surfaces of finite-element models, as do the TEM cells and triplate cells of the preceding chapter. Finally, to allow permanent magnet excitations, the third term is added that involves the distribution of the coercive field intensity \mathbf{H}_c of Chapter 5 as detailed elsewhere [1].

Note that (14.3) includes the permittance matrix times the second time derivative (indicated by the double dot) of $\{u_E\}$ and the conductance matrix times the first time

derivative (indicated by the single dot) of $\{u_E\}$. It also includes the reluctance matrix times $\{u_E\}$ as expected from Chapter 4. Because of its time derivatives, (14.3) can solve both static and dynamic (time-varying) electromagnetic problems.

The derivation of the general electromagnetic matrix equation (14.3) is based on electromagnetic energy. Instead of minimizing an energy functional as in Chapter 4, an energy variational including all forms of energy is set to zero [1, 2].

Because (14.3) includes all forms of electromagnetic energy as well as time derivatives, it can solve many types of electromagnetic problems. They are the following.

- (1) Static problems: electrostatics, magnetostatics, current flow.
- (2) AC problems, in which each dot is replaced by $j2\pi f$, where f is any frequency.
- (3) Transient problems, in which the dots involve time steps (as in Chapter 9).
- (4) Nonlinear magnetostatic problems (with nonlinear B - H curves).
- (5) Nonlinear transient problems, using time steps and nonlinear B - H curves.
- (6) Modal solutions of resonance problems, usually at high frequencies only encountered by magnetic actuators and sensors when undergoing EMC tests.

14.2 0D AND 1D FINITE ELEMENTS FOR COUPLING ELECTRIC CIRCUITS

The general formulation of (14.3) allows for 3D finite elements, 2D finite elements, and also one dimensional (1D) and zero dimensional (0D) finite elements. The 1D and 0D finite elements allow electric circuits to be included in the finite-element model. While other methods of including electric circuits are available [3], the 0D technique described here is especially easy to understand.

Zero dimensional (0D) finite elements connect nodes independent of their geometric dimensional distances [2]. Since conventional electric circuit elements R , C , and L connect circuit nodes independent of their distance and only dependent on topology, 0D finite elements can model circuit elements. Thus the general formulation (14.3) includes the three 0D finite elements labeled as res, cap, and ind in Figure 14.1. Because circuit nodes have voltage as their potential, the res, cap, and ind elements have the time integral of voltage (14.7) as their potential.

The cap 0D finite element of C farads contributes to the permittance $[M_E]$ matrix the terms:

$$[M_c] = C \begin{bmatrix} 1 & -1 \\ -1 & 1 \end{bmatrix} \quad (14.9)$$

The res 0D finite element of R ohms contributes to the conductance $[B_E]$ matrix the terms:

$$[B_R] = \frac{1}{R} \begin{bmatrix} 1 & -1 \\ -1 & 1 \end{bmatrix} \quad (14.10)$$

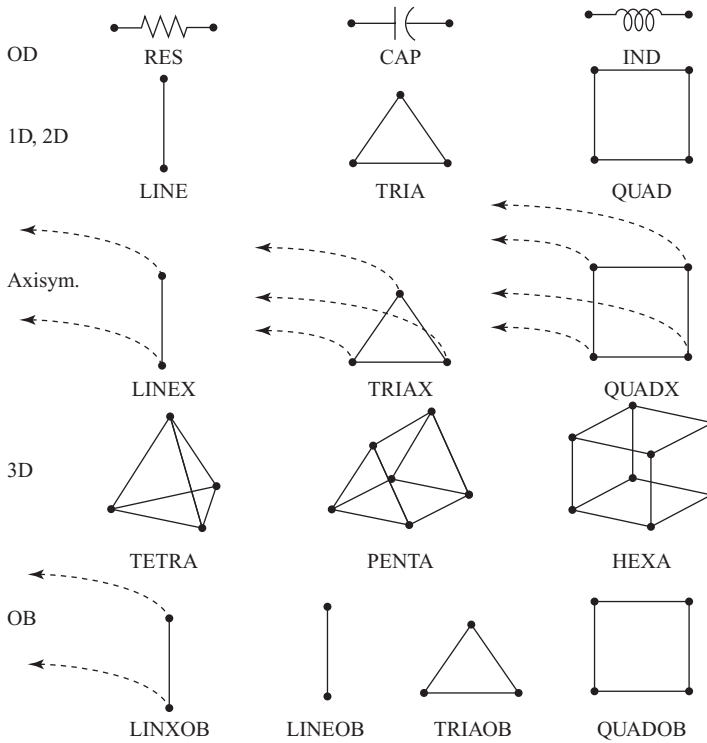


FIGURE 14.1 Finite elements of various dimensions used in the general formulation (14.3).

Finally, the ind 0D finite element of L henrys contributes to the reluctance $[K_E]$ matrix the terms:

$$[K_L] = \frac{1}{L} \begin{bmatrix} 1 & -1 \\ -1 & 1 \end{bmatrix} \quad (14.11)$$

Inserting the above three terms in (14.3) yields the equation:

$$C \frac{\partial V}{\partial t} + \frac{V}{R} + \frac{1}{L} \int V dt = I \quad (14.12)$$

where V is the voltage difference between the two nodes and I is their current. Because (14.12) agrees exactly with Kirchhoff's current law of conventional electric circuit theory for a parallel RLC circuit, the 0D finite-element method of analyzing circuits is validated.

To couple the above 0D circuit finite elements into a 3D or 2D finite-element model, 1D finite elements can be used. As shown in Figure 14.1, there are two types of 1D elements, the line and the linex. The linex is used only for axisymmetric problems, while the line is more general.

The line element usually is made highly conductive in order to represent wires and/or coils. The 1D line element can then connect 0D circuit elements into 2D or 3D finite-element models of magnetic devices. All of the available 2D and 3D finite elements are shown in Figure 14.1, including *open boundary* finite elements. The balloon boundary finite elements used in previous examples, such as Example 13.1, are one type of open boundary finite element. The types of open boundary elements shown in Figure 14.1 are called ABC elements, which stands for *asymptotic boundary condition* or (for high frequency problems) *absorbing boundary condition*. The ABC elements have the features of producing essentially no increase in computer times and serving well for static [4], transient, and AC problems [5].

Example 14.1 Constant Permeability Transformer with Impedance Loading its Secondary The transformer shown in Figure E14.1.1 is made of constant permeability laminated (zero conductivity) steel. As discussed for linear variable differential transformers (LVDTs) in Chapter 11, placing a load impedance on a transformer secondary affects transformer currents and voltages. The transformer in Figure E14.1.1 has a $1\text{-}\Omega$ resistive load impedance on its four turn secondary winding. Its one turn primary winding is excited by 120-V 60-Hz AC and has a resistance of $0.1\text{ }\Omega$. The rectangular primary and secondary windings are separated from the core by 0.25 m . The core has dimensions shown in Figure E14.1.1. Use the formulation described in the above sections to find both transformer currents for the following cases.

- The core permeability is $1.E5$ times that of air.
- The core permeability is 500 times that of air.

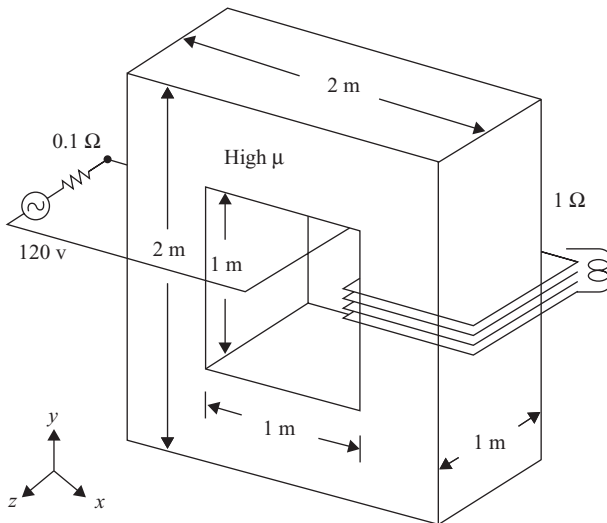


FIGURE E14.1.1 Transformer of Example 14.1.

- (c) Same as (b) but the secondary winding is made nonrectangular by reducing its separation from the primary from 0.5 to 0.25 m over one-half of its depth in the z direction.

Solution The AC methods of this chapter were used [6] to obtain the results listed in Table E14.1.1. For case (a), the currents in the row with relative permeability 1.E5 were computed, along with the flux line plot shown in Figure E14.1.2 with the visible 3D, 1D, and 0D finite elements. Note that the computed primary current I_1 and secondary current I_2 agree closely with those of an ideal transformer listed in the top row of Table E14.1.1, which have a ratio exactly equal to their turns ratio.

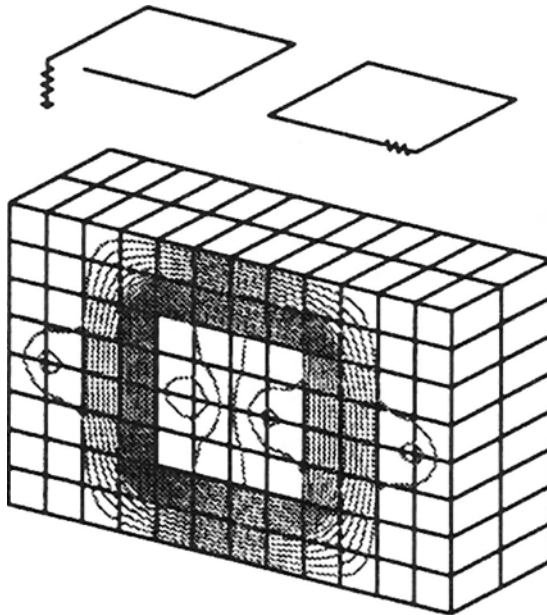


FIGURE E14.1.2 Computer display of finite-element model and computed flux lines for Example 14.1 case (a).

TABLE E14.1.1 Calculated Transformer Current Magnitudes

| Core μ_r | Secondary Coil | I_1 (A) | I_2 (A) |
|--------------|----------------|-----------|-----------|
| Infinity | Ideal | 738.4 | 184.6 |
| 1.E5 | Rectangle | 738.5 | 184.6 |
| 500 | Rectangle | 1099.1 | 93.5 |
| 500 | 3D, closer | 1098.9 | 93.6 |

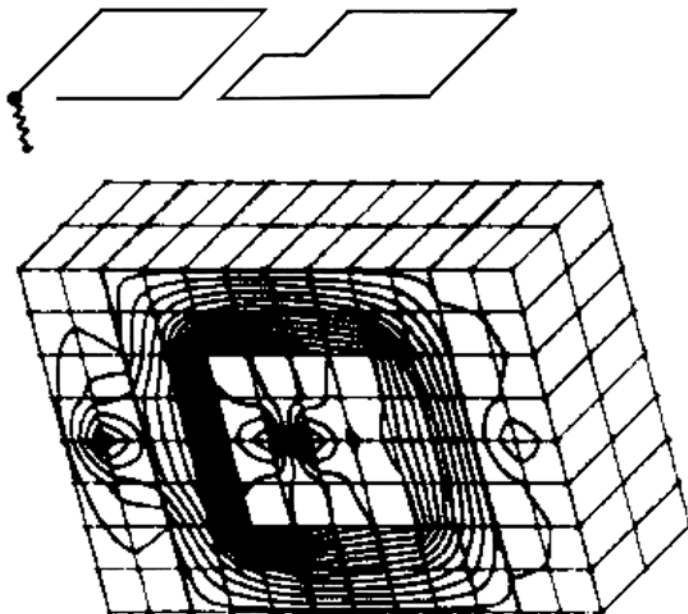


FIGURE E14.1.3 Computer display of finite-element model and computed flux lines for Example 14.1 case (c).

For cases (b) and (c), the computed currents are listed in the bottom two rows of Table E14.1.1. As expected, lowering the permeability causes the primary current to rise and the secondary current to fall. However, note that the closer coupling of the two windings of case (c) causes a slight decrease in primary current and increase in secondary current. The flux line plot of case (c) is shown in Figure E14.1.3, showing the shift in the secondary flux lines.

Example 14.2 Nonlinear Transformer Waveforms with Impedance Loading its Secondary

The transformer of Example 14.1 is now made of nonlinear steel with conductivity 1 S/m. The secondary and primary impedances remain as in Figure E14.1.1, but the primary voltage is changed from a sinusoid to the triangular waveform shown in Figure E14.2.1 of period 16 ms with 1200 V peak. This large voltage produces saturation, and the steel is assumed to have the B - H curve listed elsewhere [2]. The waveforms of steel flux density and secondary current are to be computed during two periods after the primary voltage is applied.

Solution The nonlinear transient methods of this chapter were used [6] to obtain the waveforms shown in Figures E14.2.2 and E14.2.3. Note that the flux density waveform is “clipped” at approximately 1.5 T due to saturation, as one might expect. Because the secondary voltage and current are proportional to the time derivative of flux density according to Faraday’s law, the current waveform is “peaked.” Thus saturation effects are fully computed, including the losses in the steel [6].

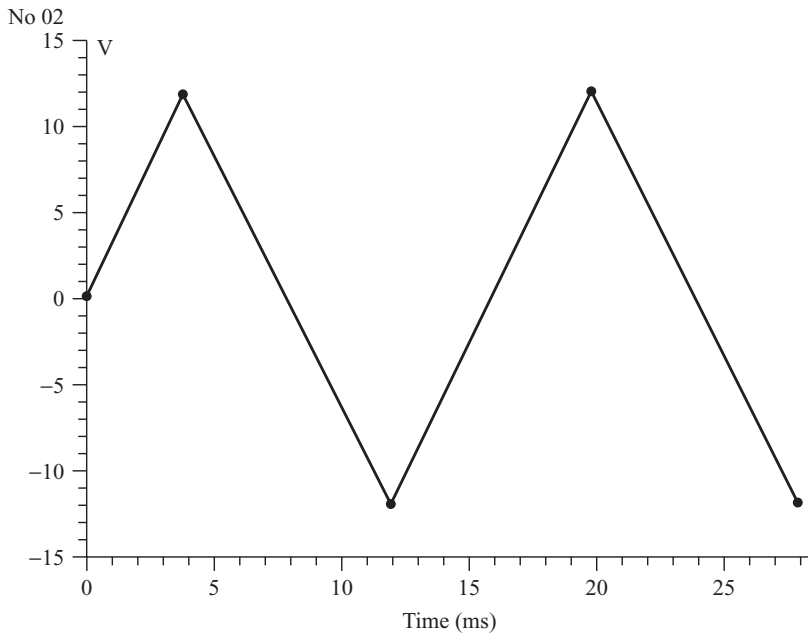


FIGURE E14.2.1 Applied primary voltage waveform for Example 14.2.

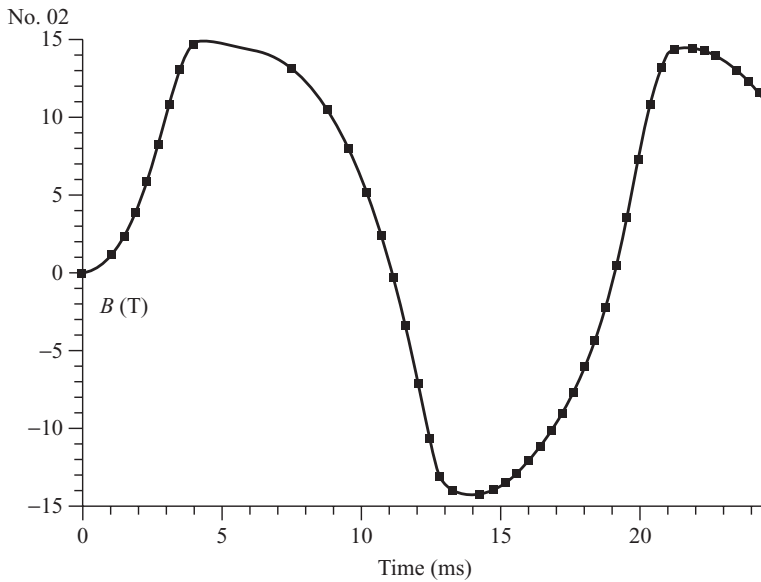


FIGURE E14.2.2 Computed flux density in transformer steel core of Example 14.2.

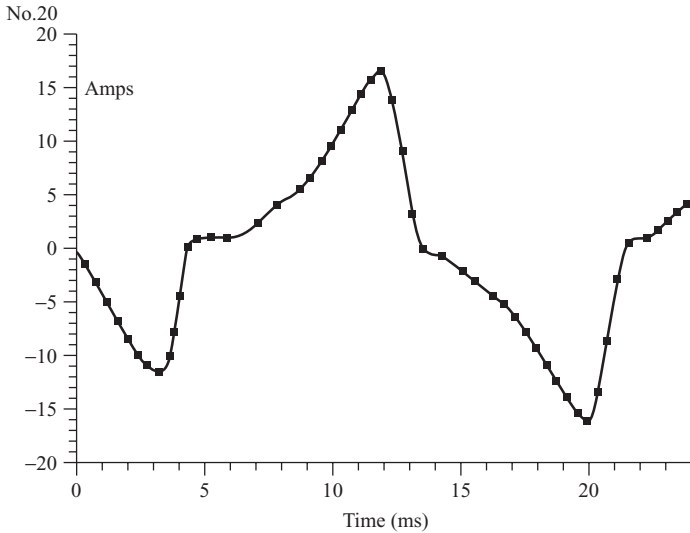


FIGURE E14.2.3 Computed secondary current waveform for Example 14.2.

14.3 STRUCTURAL FINITE-ELEMENT MATRIX EQUATION

To allow motion of the armatures of magnetic actuators and sensors, some of the electromagnetic finite elements shown in Figure 14.1 must be allowed to move. The simplest type of motion is *rigid body motion*, and it can be modeled by placing *moving surfaces* around 3D armatures. By including rigid body motion in finite-element eddy current solvers, various types of moving electromechanical devices have been analyzed [7]. Such finite-element software computes the effects of rigid body motion on eddy currents and transient electromechanical performance.

To allow nonrigid body motion, that is, deformations and stresses, structural finite elements can be used. Structural finite-element analysis is very commonly used to compute mechanical stresses and other mechanical parameters. The method, available in several commercial software packages, usually solves first for mechanical displacements (deformations), from which the stresses are then obtained.

The 3D structural finite-element formulation described here is based on three matrices: $[K_S]$, $[B_S]$, and $[M_S]$. They appear in the structural finite-element equation [2]:

$$[M_S]\{\ddot{u}_S\} + [B_S]\{\dot{u}_S\} + [K_S]\{u_S\} = \{F_S(t)\} \quad (14.13)$$

where $[K_S]$ is the mechanical stiffness matrix mentioned in Chapter 4 and is produced by springs and other elastic structures. Also, $[B_S]$ is the damping matrix due to friction and other power losses, and $[M_S]$ is the mass matrix.

The $[M_S]$ matrix term thus represents the mass times acceleration of Newton's second law of motion. The $[K_S]$ matrix term represents Hooke's law of spring force,

while the $[B_S]$ matrix term represents forces observed in dashpots. All three matrices are common to magnetic actuators and sensors. The matrices are assembled element by element, where various structural elements are available. Detailed matrix derivations for structural finite-element types such as truss, rod, bar, beam, triangular plate, quadrilateral plate, and hexahedron appear in books [2, 8].

Appendix A includes symbols, dimensions, and units of mechanics. Also, Figure 3.2 shows the key relations for a simple mechanical structure and compares them with those for magnetic circuits, electric circuits, and heat conduction.

The unknown structural vector $\{u_S\}$ in (14.13) here contains components at each finite-element node:

$$\{u_S\} = \begin{bmatrix} u_1 \\ u_2 \\ u_3 \end{bmatrix} \quad (14.14)$$

where the three components of translation \mathbf{u} in many cases are x , y , and z components, but may also be in other coordinate systems.

The right-hand side of (14.13) is the structural excitation vector, consisting of the applied forces at nodes. The forces may be produced by electromagnetic fields as described in Chapter 5.

Note that the structural equation (14.13) is directly analogous to the electromagnetic equation (14.3). Both include an $[M]$ matrix times the second time derivative (indicated by the double dot) of $\{u\}$ and a $[B]$ matrix times the first time derivative (indicated by the single dot) of $\{u\}$. They both also include a $[K]$ matrix times $\{u\}$. Because of their time derivatives, (14.3) and (14.13) can solve both static and dynamic (time-varying) problems.

14.4 FORCE AND MOTION COMPUTATION BY TIME STEPPING

Coupled electromechanical problems can be solved in the time domain by solving both (14.3) and (14.13) at each time step [9]. The two equations are coupled at each time step through their right-hand side excitation vectors. The electromagnetic excitation vector has additional terms due to motion. All finite elements can have both electromagnetic and structural material properties.

The Maxwell stress tensor is used to compute the distributed structural force produced by electromagnetic fields at surface nodes. Chapter 5 presented the component of Maxwell stress normal to a surface; the complete nonlinear stress tensor $[\tau]$ for all pressure components relates pressure and direction \mathbf{n} according to [10]:

$$\{P\} = [\tau] \{n\} \quad (14.15)$$

$$\begin{bmatrix} P_x \\ P_y \\ P_z \end{bmatrix} = \begin{pmatrix} B_x H_x - w_m & B_x H_y & B_x H_z \\ B_y H_x & B_y H_y - w_m & B_y H_z \\ B_z H_x & B_z H_y & B_z H_z - w_m \end{pmatrix} \begin{bmatrix} n_x \\ n_y \\ n_z \end{bmatrix} \quad (14.16)$$

where w_m is linear or nonlinear magnetic energy density as in Chapter 5 and n_x , n_y , and n_z are components of the unit vector \mathbf{n} normal to the surface. Integrating the above pressure over a closed surface s gives the force component F_{Si} in the direction i [10]:

$$F_{Si} = \oint (\tau_{ij} n_j) ds \quad (14.17)$$

Thus

$$\frac{F_{Si}}{s} = P_i = \tau_{ij} n_j \quad (14.18)$$

Substituting (14.16) gives the pressure in terms of normal N and tangent T components of the magnetic fields [10]:

$$P_N = B_N H_N - w_m; \quad P_T = B_T |H_N| \quad (14.19)$$

As shown in Figure 14.2 [10], there are two ways of computing magnetic force on an object. The first method is to completely surround the object with the surface, such as the armature of a magnetic actuator. This one-sided integration method

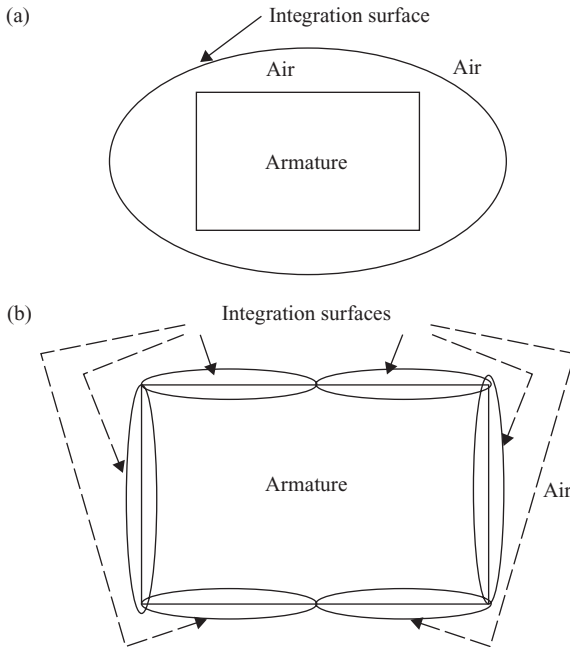


FIGURE 14.2 Integration surfaces for Maxwell stress tensor computation. (a) one-sided integration, (b) two-sided integration.

obtains the total force on the armature, but not its distribution. The second method is to place multiple integration surfaces encompassing both steel and air sides of all finite elements on the armature surface. As these integration regions are collapsed to the armature surface, they perform two-sided integrations along the armature face. Because of the higher \mathbf{H} field and magnetic energy density in air, the force on steel and other high permeability materials is outward toward the higher energy density air region. Also, if steel has regions of varying saturation, the two-sided integrations can be carried out at finite-element interfaces within the steel. Thus the two-sided method computes the spatial *distribution* of force, which is helpful in understanding actuator behavior and is essential in obtaining mechanical stresses.

As the motion proceeds, nodes can move. In the examples given below, air is modeled with a very low modulus of elasticity of 1 Pa, which produces very small contributions to the $[K_S]$ matrix. Thus the air elements easily collapse or expand as motion occurs. If the motion is very large, then some air elements may become very distorted, which reduces their accuracy. For large motion, it may be necessary to not only move nodes but also reconnect the nodes through new finite elements.

14.5 TYPICAL ELECTROMECHANICAL APPLICATIONS

In the examples below the motion is small enough that no element reconnection is required. All results are obtained by time stepping using both nonlinear electromagnetic and structural finite elements. All eddy current effects, including motional EMFs, are included in the solutions. While in structural finite-element analysis air is rarely modeled, air finite elements are here required for electromagnetic fields and also appear in the structural finite-element model. The key parameter usually needed for magnetic actuators and sensors is response time, which is computed as follows by electromagnetic and structural finite elements.

14.5.1 DC Solenoid with Slowly Rising Current Input

The Bessho DC axisymmetric plunger solenoid actuator of Figure 5.2 has been previously studied in Chapters 5, 7, 9, and 12. As mentioned in Chapter 12, its time constant is 20 ms according to the original paper by Bessho et al. [11]. The current waveform applied in the Bessho experimental tests obeys:

$$I(t) = I_{DC}(1 - e^{-t/0.020}) \quad (14.20)$$

where the final current I_{DC} is 0.5 A during the experimental tests.

To compute the motion of this actuator, the finite-element model shown in Figure 14.3 is made with all elements having both electromagnetic and structural properties [9]. The steel finite elements are given a modulus of elasticity of 200.E9 Pa and Poisson's ratio of 0.265, as typical for many steels [2]. As mentioned previously, the electromagnetic steel elements have nonlinear B - H curves and electrical conductivity of 1.7E6 S/m. The air finite elements are given a structural modulus of

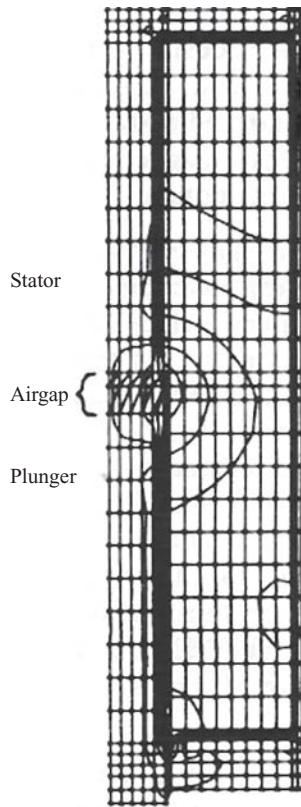


FIGURE 14.3 Computer display of coupled electromagnetic and structural finite-element model of Bessho magnetic actuator with applied current. The computed flux lines are shown at 5 ms for the 15-mm airgap.

elasticity of 1 Pa. Initial airgaps are set to match the experimental tests at 10, 15, and 20 mm. As set in the experiments, the total moveable mass is 6 kg.

The computed position of the armature versus time is shown in Figure 14.4 for all three initial airgaps [9]. Also shown in Figure 14.4 are the corresponding measured position curves. Note that computations and measurements agree quite well. The largest disagreement is for the 20-mm airgap, which produces the greatest node motion and element distortion. Note that the time to close, often the most important parameter for magnetic actuators, is accurately predicted by the coupled finite-element analysis.

14.5.2 DC Solenoid with Step Voltage Input

Like most DC actuators, the Bessho solenoid is most likely to be excited by a DC voltage step. As mentioned in Chapter 12, the time constant of the Bessho solenoid of 20 ms is unchanged even if its number of turns is changed. However, it is important

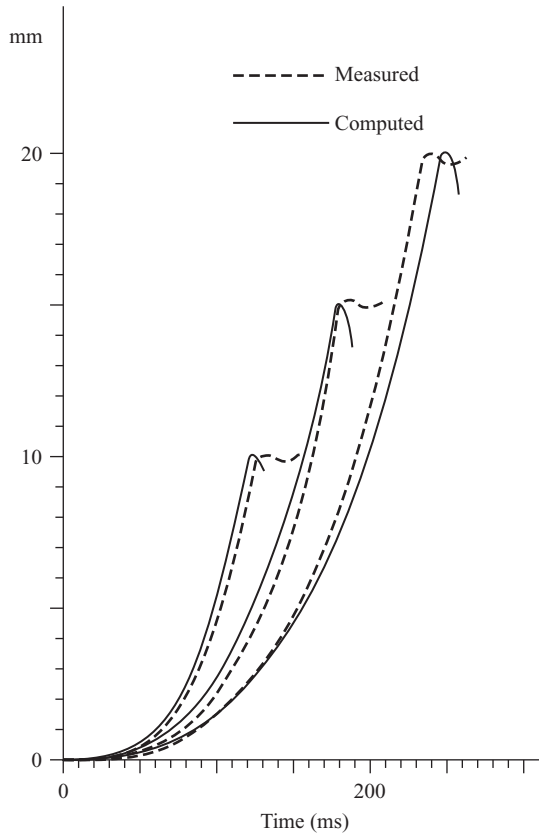


FIGURE 14.4 Displacement of armature versus time for initial airgaps of 10, 15, and 20 mm. All curves are for the applied current waveform of (14.19) with 0.5-A DC and total moving mass of 6 kg.

to note that the current waveform of (14.19) is based upon conventional LR circuit theory and does not include the effects of motional EMF. As we shall see, when a voltage is applied, *motion effects can change the current waveform and thus change the actuator response time.*

To apply a voltage, 0D and 1D finite elements are added to Figure 14.3, producing the finite-element model shown in Figure 14.5 [12]. The 0D element is a resistor of value $200\ \Omega$, and it is driven by a step voltage source of 100 V. The final DC current is $100\text{ V}/200\ \Omega = 0.5\text{ A}$, the desired value. The initial airgap is assumed to be 10 mm.

The computed current versus time is shown in Figure 14.6 [12]. Note that for times less than 40 ms, the current increases exponentially with a time constant of approximately 20 ms as in Section 12.2. However, from approximately 40 to 120 ms, the current *decreases* due to the motional voltage produced by the moving armature. The computed armature position versus time is approximately the same as the 10-mm curve in Figure 14.4, which shows substantial motion beginning at approximately

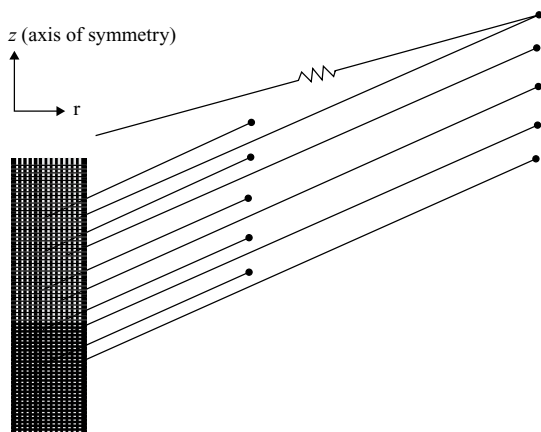


FIGURE 14.5 Coupled electromagnetic and structural finite-element model of Bessho magnetic actuator with applied voltage. Note that the circuit is distributed over 10 points within the coil area.

40 ms. At approximately 117 ms, the armature reaches closure and thus at that time the current of Figure 14.6 dips to a minimum. Beyond that time, the current rises again, but with a different slope than before, because L has changed with armature position. The current dip at closure is sometimes used to sense closure.

The above computations are for measured steel conductivity of $1.7\text{E}6$ S/m. To examine the effects of conductivity on actuator speed, conductivity σ was varied as

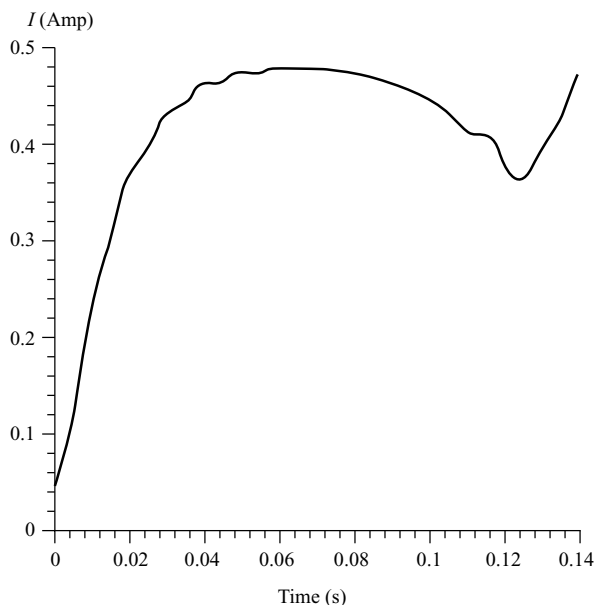


FIGURE 14.6 Computed current versus time for Bessho actuator with applied step voltage.

TABLE 14.1 Closing Times (ms)^a Computed Using Electromechanical Finite Elements for Various Step Excitations of V or I , Conductivities σ , and Mechanical Parameters

| Case | $\sigma = 0$ | % | $\sigma = 1.7\text{E}6$ | % | $\sigma = 5\text{E}6$ | % | $\sigma = 10\text{E}6$ | % |
|-------------------------|--------------|---|-------------------------|------------|-----------------------|------|------------------------|------|
| 1. V , 6 kg | 115 | 0 | <u>117</u> | <u>1.7</u> | 121 | 5.2 | 126 | 9.6 |
| 2. V , 1.4 kg | 67 | 0 | <u>72</u> | <u>7.5</u> | 75 | 11.9 | 80 | 19.4 |
| 3. I , 1.4 kg | 46 | 0 | 51 | 10.9 | 56 | 21.7 | 62 | 34.8 |
| 4. I , 1.4 kg, spring | 49 | 0 | 54 | 10.2 | 61 | 24.5 | 67 | 36.7 |

^aThe percentage changes in closing times due to eddy currents are computed, with Bessho's baseline case underlined.

listed in Table 14.1. Besides varying σ from 0 to 10.E6 S/m, four different cases are examined in the table. Case 1 is the voltage step examined in Figure 14.6; it shows that varying conductivity only varies closing time by about 11 ms. In case 2, the moving mass is lowered to the armature mass only, which is 1.4 kg. In case 3, the 0.5-A current is input as a step at time zero, producing the fastest closing times, especially for zero conductivity. Finally, in case 4 a small opposing spring of 1500 N/m is added, typical of relay spring forces [13].

14.5.3 AC Clapper Solenoid Motion and Stress

The Eaton 60-Hz AC clapper solenoid actuator of Figures 4.3 and 8.4 can be analyzed using coupled nonlinear electromagnetic and structural finite elements. The spring in Figure 4.3 is made up of multiple steel coils and relay leaves, which interact to produce the nonlinear spring force versus position curve shown in Figure 14.7. When the armature is in the open position with the 5.97-mm airgap of Figure 4.3, the spring is partially compressed to produce a preload of 2.55 N. The slope of Figure 14.7, called K_{Snl} , varies from as low as 443 N/m to as high as 3.E4 N/m [14]. When the

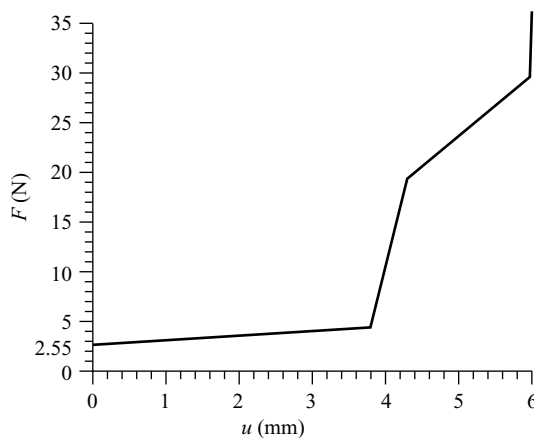


FIGURE 14.7 Measured nonlinear spring curve of actuator spring and relay of Eaton AC actuator.

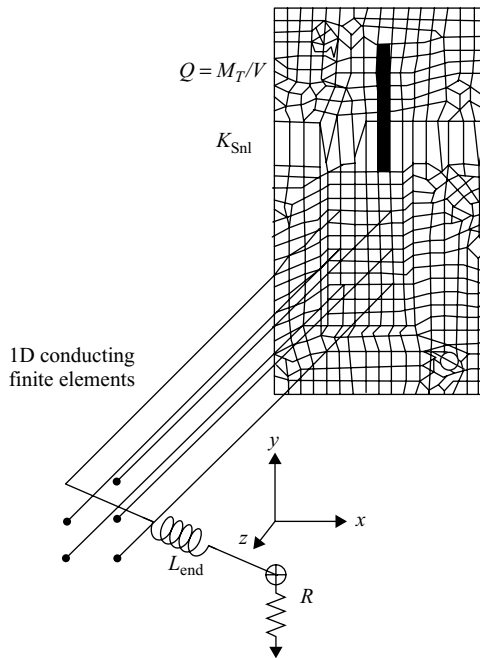


FIGURE 14.8 Coupled finite-element model of right-half of Eaton AC actuator.

airgap is closed at 5.97 mm, the slope in Figure 14.7 becomes very high to prevent further motion.

The nonlinear spring K_{Snl} is included in the coupled finite-element model shown in Figure 14.8. Just as for the Bessho actuator, the total moving mass M_T is somewhat greater than simply the mass of the magnetic armature. Thus the mass density ρ of the armature structural finite elements is set to M_T divided by the armature volume. The steel 2D finite elements have the same structural properties as in the Bessho actuator, with modulus of elasticity 2.E11 Pa and Poisson's ratio of 0.265.

The electromagnetic finite-element model is also shown in Figure 14.8, and consists of 0D, 1D, and 2D finite elements. The 2D finite-elements model the nonlinear steel, the air, the coil area, and the aluminum shading ring. To account for 3D end resistance of the shading ring, the aluminum conductivity is reduced somewhat [14]. Figure 14.8 also contains six 1D line finite elements modeling the coil, which are attached to 0D finite elements modeling the coil R and end turn inductance L_{end} . The end turn inductance computed using 3D finite elements is 23 mH [14]; adding it to the 2D model of Figure 14.8 ensures accurate results with minimal computer time. The model of Figure 14.8 ignores AC hysteresis losses in the steel, but if they are significant they can be included [15].

The time required for closure of AC actuators depends on the instant within the AC cycle that the voltage is applied. Here the voltage applied at time zero is assumed to be zero and to rise thereafter as a sine wave. The resulting computed current

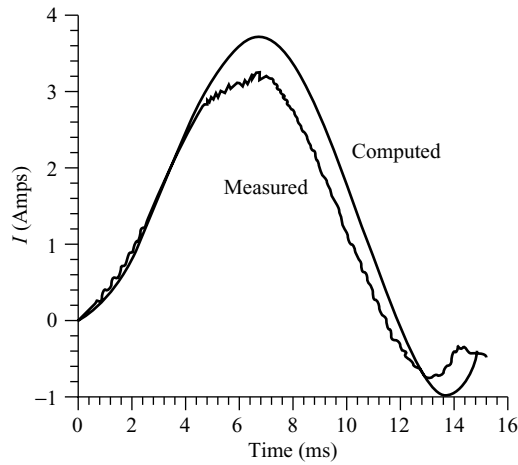


FIGURE 14.9 Coil current waveform of Eaton AC actuator.

versus time is shown in Figure 14.9. The measured current is also shown and agrees reasonably well.

The computed armature displacement versus time is shown in Figure 14.10. The leftmost curve is for an armature density ρ equal to 0.22 kg divided by the model armature volume v . However, it was realized later that the potentiometer used to trace the measured curve in Figure 14.10 added to the moving mass and produces $M_T = 0.267$ kg. Increasing the armature density accordingly yields the rightmost curve in Figure 14.10, which agrees very closely with the measured curve. It should be noted that the force of gravity is also included in Figure 14.10 because the actuator

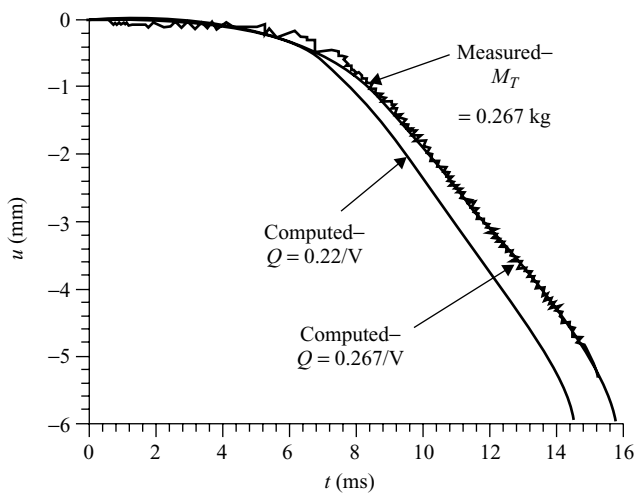


FIGURE 14.10 Position versus time for Eaton AC actuator mounted vertically.

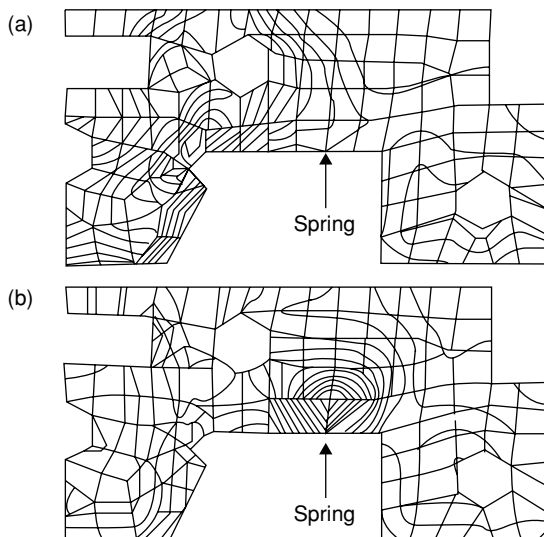


FIGURE 14.11 Eaton armature finite elements and stress contours (also available in color). (a) at $t = 15.6$ ms, maximum = 943 kPa, (b) at $t = 12$ ms, maximum = 26 kPa.

is mounted vertically. Both the computed and measured closure times in Figure 14.10 are 16.0 ms.

Besides computing the electrical and mechanical responses of Figures 14.9 and 14.10, the coupled finite-element analysis also obtains mechanical stresses. A common parameter for stress is called Von Mises equivalent stress [2], and it is plotted for the armature in Figure 14.11. The stress varies with time and with assumed spring position. The maximum stress in Figure 14.11 is 943 kPa, which is too low to cause yield or other mechanical failure of most steels. However, improper placement of bolt holes might increase the stresses and produce mechanical failure. Hence computed stress distributions can be very valuable to design engineers [16].

Since the stresses and strains of the steel armature are quite small, its deformations are also small, only a few microns at most. However, armatures of magnetic actuators are sometimes purposely made of flexible material which deforms greatly during actuation. Examples of flexible armatures are common in *magnetic switches*, including flexible reeds in *reed switches* used as relays and sensors [17, 18], and flexible ferrite rubber permanent magnets used to latch push-button switches [19].

14.5.4 Transformers with Switches or Sensors

Magnetic actuators and sensors are often driven by electronic circuits, which usually require nonlinear modeling. The simplest type of nonlinear behavior is a switch. An ideal open switch has zero current, but its voltage drop is unknown. An ideal closed switch has zero voltage, but its current is unknown.

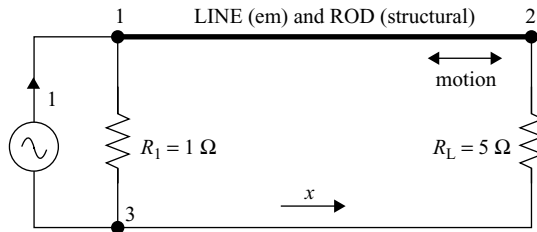


FIGURE 14.12 Time-varying resistor.

A switch is thus a time-varying resistor, which can be modeled using 1D coupled electromagnetic and structural finite elements [20, 21]. The 1D finite element in Figure 14.12 is a typical variable resistor. It behaves as a line electromagnetic finite element of Figure 14.1 and also as a 1D structural rod element. To vary the resistance, the line is stretched by applying a mechanical force that varies with time. For example, if the line has a conductivity of 1 S/m and initial length of 1 cm, then its resistance is only 0.01 Ω initially. Applying a large force to stretch the line length to 1 km, its resistance increases to 1 k Ω .

Such a switch is attached to the transformer secondary shown in Figure 14.13. Its primary is excited by a 50-Hz triangular wave. If the switch is always closed, the 86 m Ω secondary resistor has the computed voltage shown in Figure 14.14 over time from 0 to 25 ms. If the switch is opened, however, from time 15 to 20 ms, the secondary current is zero during that period but shows an inductive “kick” when reclosed in Figure 14.15.

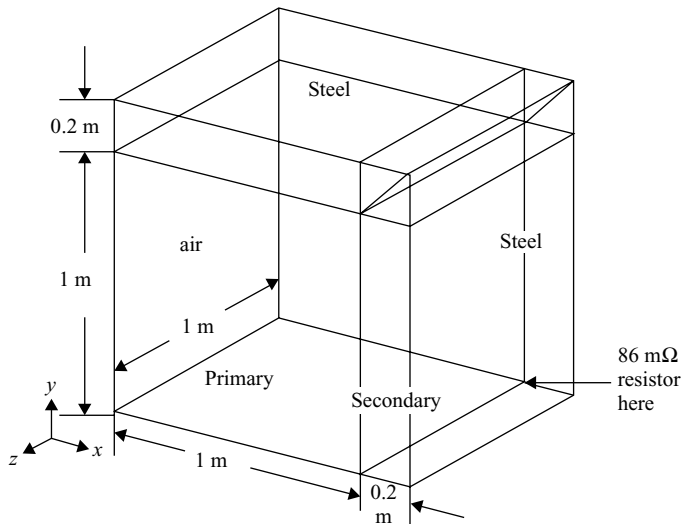


FIGURE 14.13 Transformer with secondary 86 m Ω resistor that may be switched in or out. One-quarter of the transformer is shown, with its primary and secondary coils modeled by 1D line finite elements.

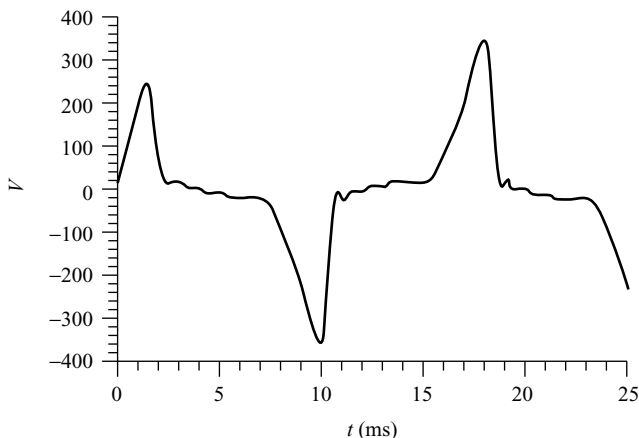


FIGURE 14.14 Computed secondary resistor voltage for transformer of Figure 14.13 when secondary switch is always closed.

Such variable resistance models can be useful for modeling electronically controlled actuators and sensors. For example, LVDTs of Chapter 11 can have varying load impedances, and magnetoresistive sensors of Chapter 10 typically behave as time-varying resistors.

14.5.5 Reciprocating Magnetic Actuators

Springs are very commonly employed in magnetic actuators to provide return force. Examples (other than the Eaton clapper actuator) include *reciprocating magnetic*

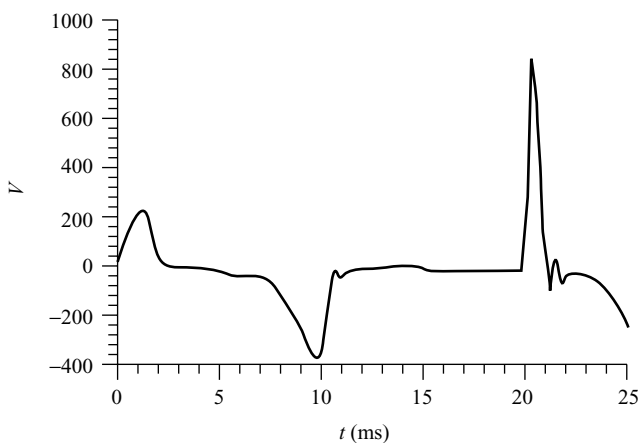


FIGURE 14.15 Computed secondary voltage for transformer of Figure 14.13 when secondary switch is closed except during time from 15 to 20 ms.

actuators. They produce repeated back-and-forth linear motion by alternately supplying coil current to provide magnetic force and motion in one direction, and removing (or in some designs reversing) the coil current to allow the spring to move the armature back. Door bells have long been a common example.

Nowadays new types of reciprocating magnetic actuators are being developed for applications such as shakers [22] and piston compressors [23]. Ordinarily most compressor pistons are driven by rotary motors via crankshafts, connecting rods, and wrist pins. These three mechanical parts are eliminated by use of a reciprocating actuator (also often called a reciprocating motor). A new reciprocating magnetic actuator designed for operating compressors for refrigeration is shown in Figure 14.16. Its outer stator has coil windings that are fed with AC voltage and current. Preferably the frequency of the current is the readily available 60 Hz or 50 Hz. The armature in Figure 14.16 has NdFeB permanent magnets mounted on a nonpermeable tube. The actuator design is somewhat similar to a much older design [24] which had difficulty controlling its stroke and thus the compression ratio. Accurate control of stroke is much easier nowadays using modern magnetic sensors and feedback control electronics.

The mechanical resonant frequency of the simple spring-mass system of the armature of Figure 14.16 is derived from (14.13) to be:

$$f_{\text{res}} = (1/(2\pi))(K/M)^{1/2} \quad (14.21)$$

where K is the armature spring constant and M is the total reciprocating mass. This resonant frequency is designed to match the AC drive frequency for maximum efficiency of the compressor system [23].

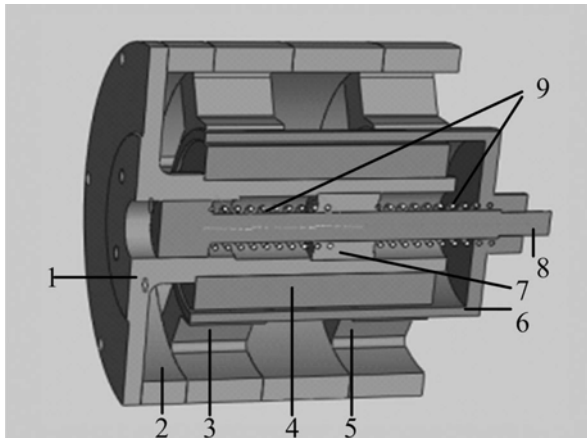


FIGURE 14.16 Reciprocating magnetic actuator for a compressor [23]. Parts are: (1) compression chamber, (2) outer shell, (3) left outer steel stator with copper winding (not shown), (4) inner steel stator, (5) right outer stator, (6) permanent magnet armature, (7) linear bearing, (8) piston in compression chamber, (9) spring with spring constant K .

PROBLEMS

- 14.1** The transformer of Example 14.1 can also be analyzed using its equivalent electrical circuit. As discussed in Chapter 8, a coil with losses is equivalent to a resistor in parallel with an inductor. From Chapter 5, the parallel magnetizing inductor equals the square of the primary turns divided by the reluctance. The secondary resistor must be referred to the primary according to ideal transformer theory. Calculate the reluctance for relative steel permeability of 1.E5 and the resulting magnetizing inductor. Then use the inductor to calculate the currents and compare them with the finite element computations of case (a).
- 14.2** Extend Problem 14.1 for case (b) of Example 14.1. That is, let the steel relative permeability be 500 and compare your calculated currents with the finite-element computations of case (b).

REFERENCES

1. MacNeal BE, Brauer JR, Coppelino RN. A general finite element vector potential formulation of electromagnetics using a time-integrated electric scalar potential. *IEEE Trans Magn* 1990;26:1768–1770.
2. Brauer JR (ed.). *What Every Engineer Should Know About Finite Element Analysis*, 2nd ed. New York: Marcel Dekker, Inc.; 1993.
3. Zhou P, Fu WN, Lin D, Stanton S, Cendes ZJ. Numerical modeling of magnetic devices. *IEEE Trans Magn* 2004;40:1803–1809.
4. Brauer JR, Schaeffer SM, Lee J-F, Mittra R. Asymptotic boundary condition for three dimensional magnetostatic finite elements. *IEEE Trans Magn* 1991;27:5013–5015.
5. Brauer JR, Mittra R, Lee J-F. Absorbing boundary condition for vector and scalar potentials arising in electromagnetic finite element analysis in frequency and time domains. *Proceedings of the IEEE Antennas and Propagation Society Symposium*, July 1992, pp 1224–1227.
6. Brauer JR, MacNeal BE, Hirtenfelder F. New constraint technique for 3D finite element analysis of multiturn windings with attached circuits. *IEEE Trans Magn* 1993;29:2446–2448.
7. Zhou P, Stanton S, Cendes ZJ. Dynamic modeling of electric machines. *Proceedings of the Naval Symposium on Electrical Machines*, October 26–29, 1998, Annapolis, MD, pp 43–49.
8. MacNeal RH. *Finite Elements: Their Design and Performance*. New York: Marcel Dekker, Inc.; 1994.
9. Brauer JR, Ruehl JJ. 3D coupled nonlinear electromagnetic and structural finite element analysis of motional eddy current problems. *IEEE Trans Magn* 1994;30:3288–3291.
10. Brauer JR, Ruehl JJ, Juds MA, Van der Heiden MJ, Arkadan AA. Dynamic stress in magnetic actuator computed by coupled structural and electromagnetic finite elements. *IEEE Trans Magn* 1996;32:1046–1049.

11. Bessho K, Yamada S, Kanamura Y. Analysis of transient characteristics of plunger type electromagnets. *Electr Eng Jpn* 1978;98:56–62.
12. Brauer JR, Ruehl JJ, Hirtenfelder F. Coupled nonlinear electromagnetic and structural finite element analysis of an actuator excited by an electric circuit. *IEEE Trans Magn* 1995;31:1861–1864.
13. Brauer JR, Chen QM. Alternative dynamic electromechanical models of magnetic actuators containing eddy currents. *IEEE Trans Magn* 2000;36:1333–1336.
14. Juds MA, Brauer JR. AC contactor motion computed with coupled electromagnetic and structural finite elements. *IEEE Trans Magn* 1995;31:3575–3577.
15. Bottauscio O, Chiampi M, Manzin A. Advanced model for dynamic analysis of electromechanical devices. *IEEE Trans Magn* 2005;41:36–46.
16. Overbye V, Brauer J, Bodine P. *Blazing Trails—Finite Element Pioneers in Milwaukee*. Lincoln, NE: Writers Club Press of iUniverse, Inc.; 2002.
17. Reed switch basics. *Machine Design* 2004;48.
18. Ota T, Hirata K, Yamaguchi T, Kawase Y, Watanabe K, Nakase A. Dynamic response analysis of opening and closing sensor for windows. *IEEE Trans Magn* 2005;41:1604–1607.
19. Van Zeeland T. Magnets in switch design. *Magn Bus Technol* 2004;22–23.
20. Brauer JR, Ruehl JJ. Finite element modeling of power electronic circuits containing switches attached to saturable magnetic components. *IEEE Trans Energy Convers* 1999;14:589–594.
21. Brauer JR. Time-varying resistors, capacitors, and inductors in nonlinear transient finite element models. *IEEE Trans Magn* 1998;34:3086–3089.
22. Peng M-T, Flack TJ. Numerical analysis of the coupled circuit and cooling holes for an electromagnetic shaker. *IEEE Trans Magn* 2005;41:47–54.
23. Zhang Y, Lu Q, Yu M, Ye Y. A novel transverse-flux moving-magnet linear oscillatory actuator. *IEEE Trans Magn* 2012;48:1856–1862.
24. Brauer JR. Reciprocating linear motor. U.S. Patent 4002935, 1977.